

SOLAR CELLS

Nanoscale localized contacts for high fill factors in polymer-passivated perovskite solar cells

Jun Peng^{1*}, Daniel Walter^{1*}, Yuhao Ren², Mike Tebyetekerwa¹, Yiliang Wu¹, The Duong¹, Qiaoling Lin², Juntao Li^{2†}, Teng Lu³, Md Arafat Mahmud¹, Olivier Lee Cheong Lem⁴, Shenyao Zhao¹, Wenzhu Liu⁵, Yun Liu³, Heping Shen¹, Li Li⁴, Felipe Kremer⁶, Hieu T. Nguyen¹, Duk-Yong Choi⁷, Klaus J. Weber¹, Kylie R. Catchpole^{1†}, Thomas P. White^{1†}

Polymer passivation layers can improve the open-circuit voltage of perovskite solar cells when inserted at the perovskite–charge transport layer interfaces. Unfortunately, many such layers are poor conductors, leading to a trade-off between passivation quality (voltage) and series resistance (fill factor, FF). Here, we introduce a nanopatterned electron transport layer that overcomes this trade-off by modifying the spatial distribution of the passivation layer to form nanoscale localized charge transport pathways through an otherwise passivated interface, thereby providing both effective passivation and excellent charge extraction. By combining the nanopatterned electron transport layer with a dopant-free hole transport layer, we achieved a certified power conversion efficiency of 21.6% for a 1-square-centimeter cell with FF of 0.839, and demonstrate an encapsulated cell that retains ~91.7% of its initial efficiency after 1000 hours of damp heat exposure.

The rise in perovskite solar cell (PSC) performance has been marked by substantial increases in open-circuit voltage (V_{oc}), short-circuit current (J_{sc}), and fill factor (FF), as illustrated in Fig. 1 for reported values since 2014 (1–9). The steady increase in V_{oc} from ~1 to ~1.2 V (for simplicity, we ignore bandgap differences between the record cells) reflects efforts to reduce nonradiative recombination, especially at the perovskite–charge transport layer interfaces (10–25). For example, insertion of ultrathin passivation layers at one or both interfaces can lead to voltage gains of >100 mV in some cases (11, 22). Reported passivation materials include insulating (10–14) and semiconducting (15–17) organic materials, inorganic dielectrics (18, 19), and low-dimensional perovskites (20–25). Insulating organic materials and low-dimensional perovskites have provided some of the largest efficiency gains.

Two other important trends can be seen in Fig. 1. First, the J_{sc} of record cells has not in-

creased substantially since 2015; a consequence of the near-unity internal quantum efficiency and low optical losses of state-of-the-art cells. Second, record FF values plateaued between 2015 and 2018, before a steep increase in 2019, despite the almost linear improvement in V_{oc} during the same period. Given that FF quantifies voltage and current losses at the maximum power point relative to the maximum values of both V_{oc} and J_{sc} , the theoretical FF limit is a function of V_{oc} and depends both on the active layer bandgap and the rate of nonradiative recombination that degrades V_{oc} . In practice, however, many cells perform well below this limit because of parasitic resistive losses (shunt and series). Thus, achieving a very high FF requires low recombination losses (high V_{oc}); smooth, uniform, and dense active layers (high shunt resistance); and very efficient charge extraction and transport (low series resistance). The lack of correlation between V_{oc} and FF in Fig. 1 suggests that the FF of record cells is not limited by recombination but rather by resistive losses. Indeed, the theoretical maximum FF for a solar cell with $V_{oc} = 1.1$ V is ~0.89, well above the highest values achieved so far.

Maximizing both V_{oc} and FF is a challenge faced by all high-efficiency solar cells because of the difficulties in reducing interface recombination without hindering charge extraction. This challenge is most apparent in the case of insulating and dielectric passivation layers that provide outstanding passivation of defects [e.g., SiO_2 passivation layers in Si cells (26) or poly(methyl methacrylate) (PMMA) passivation of perovskite cells (10)] but must be extremely thin to avoid detrimental FF losses from series resistance. As an extreme example, silicon solar cells with tunnel oxide passivated contacts can experience a 70% drop in FF for a

5-Å variation in oxide thickness (27). There are many examples for PSCs showing trade-offs between passivation quality (V_{oc}) and FF, not only for ultrathin layers of insulating polymers such as polystyrene and PMMA (10–12), but also for poorly conducting, low-dimensional perovskite passivation layers (20–25). Overcoming this trade-off with new materials or device architectures could improve PSC performance.

A further challenge facing perovskite technology is maintaining high efficiency, specifically FF, on larger cell areas (5, 6, 28, 29). The record efficiencies quoted above are for very small cells (~0.1 cm^2) that are at least three orders of magnitude smaller than commercial Si cells. Increasing cell area increases the possibility of shunts created by film imperfections, whereas series resistance losses scale quadratically with current. Both contributions can rapidly degrade FF as cell areas increase, with record 1- cm^2 cells typically exhibiting FF values between 5 and 10% lower than their smaller counterparts (5).

In this work, we present a PSC architecture in which we replaced the commonly used mesoporous TiO_2 (meso- TiO_2) electron transport layer (ETL) with a sparse array of nanoscale TiO_2 cylinders (nanorods). The resulting nanopatterned ETL-perovskite interface could be effectively passivated with an ultrathin polymer passivation layer to achieve high V_{oc} that maintained outstanding charge collection and interfacial transport properties; this resulted in low series resistance and a high FF. This approach was demonstrated on a large-area (1- cm^2) cell with a certified power conversion efficiency (PCE) of 21.6% and FF = 0.839. A champion small-area (~0.165- cm^2) cell achieved a PCE of ~23.17% with $V_{oc} = 1.240$ V and FF = 0.845. We investigated and explained the performance of the nanostructured interface using three-dimensional (3D) numerical simulations that replicated accurately the FF enhancement and the observed experimental trends with nanopattern geometry. The simulations strongly suggested that the TiO_2 nanorods are incompletely coated with the PMMA:PCBM (phenyl- C_{61} -butyric acid methyl ester) passivation material, leaving exposed regions of local low-resistance contact directly analogous to local contact structures in high-efficiency silicon solar cells (30, 31). Detailed comparisons between simulation and experiment placed plausible bounds on the nanorod area fraction that was left exposed and the density of recombination-active defects at this exposed ETL-perovskite interface. In addition to the nanopatterned ETL, we also introduce here an ionic dopant-free, blended hole transport layer (HTL) that offers similar cell performance to doped alternatives such as 2,2',7',7'-tetrakis(*N*,*N*-di-4-methoxyphenylamino)-9,9'-spirobifluorene (Spiro-OMeTAD) and poly(triaryl

¹Research School of Electrical, Energy and Materials Engineering, The Australian National University, Canberra Australian Capital Territory 2600, Australia. ²State Key Laboratory of Optoelectronics Materials and Technologies, School of Physics, Sun Yat-sen University, Guangzhou 510275, China. ³Research School of Chemistry, The Australian National University, Canberra Australian Capital Territory 2600, Australia. ⁴Australian National Fabrication Facility, Research School of Physics, The Australian National University, Canberra Australian Capital Territory 2600, Australia. ⁵Research Center for New Energy Technology, Shanghai Institute of Microsystem and Information Technology, Chinese Academy of Sciences, Jiading, Shanghai 201800, China. ⁶Centre for Advanced Microscopy, The Australian National University, Canberra Australian Capital Territory 2600, Australia. ⁷Australian National Fabrication Facility, The Australian National University, Canberra Australian Capital Territory 2600, Australia. *These authors contributed equally to this work. †Corresponding author. Email: lijit3@mail.sysu.edu.cn (J.L.); kylie.catchpole@anu.edu.au (K.R.C.); thomas.white@anu.edu.au (T.P.W.)

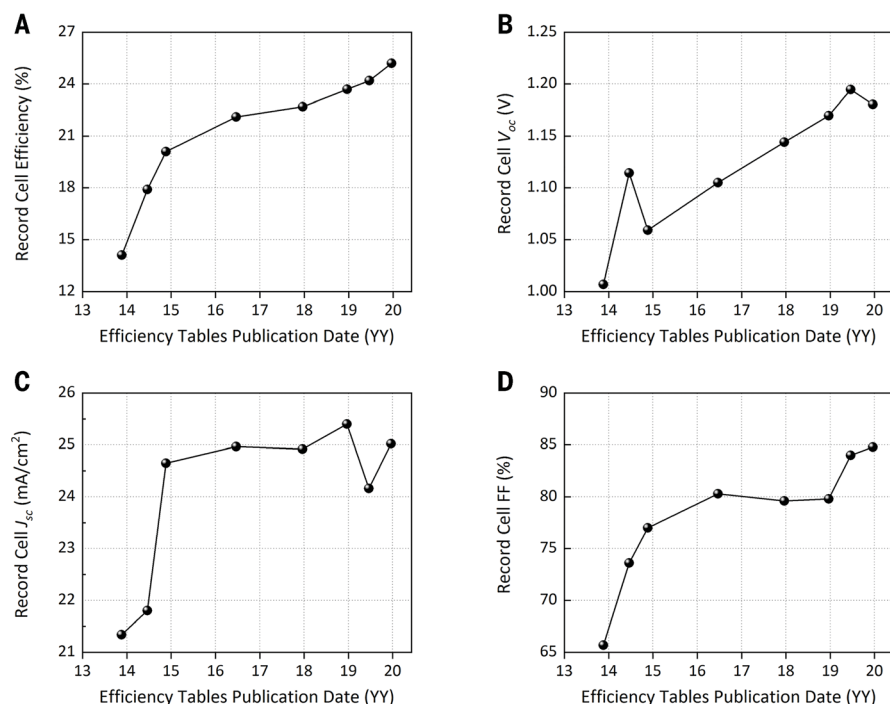


Fig. 1. Certified performance of record PSCs. (A) Record cell efficiency. (B) Record cell V_{oc} . (C) Record cell J_{sc} . (D) Record cell FF. Note that the effective area of all record cells plotted here was $<0.2 \text{ cm}^2$.

amine) (PTAA) but with much improved thermal stability. Encapsulated cells incorporating the new ETL and HTL combination retained $>90\%$ of their initial efficiency after 1000 hours of exposure to damp heat conditions of 85°C and 85% relative humidity.

Spiro-OMeTAD and PTAA are the most widely used HTL materials for high-efficiency n-i-p architecture PSCs. These layers are typically doped with bis(trifluoromethane)sulfonamide lithium salt (Li-TFSI) to improve the conductivity, but the hygroscopic Li-TFSI can accelerate moisture-induced perovskite degradation, and diffusion of Li ions throughout the cell further reduces performance and stability (6, 32, 33). These detrimental effects are exacerbated by high temperatures, contributing to the poor thermal stability of many perovskite cells. Alternative HTL layers that offer similar efficiency performance without affecting stability include poly(3-hexylthiophene) (P3HT), a semiconducting polymer used extensively in organic optoelectronics but only recently reported as an effective HTL for PSCs (6, 34, 35). Controlling the morphology and crystallinity of the P3HT film is essential for achieving a high charge carrier mobility without dopants. The hole mobility can range from $\sim 10^{-5} \text{ cm}^2 \text{ V}^{-1} \text{ s}^{-1}$ in an amorphous film up to $\sim 0.1 \text{ cm}^2 \text{ V}^{-1} \text{ s}^{-1}$ for a crystalline film with optimized π - π stacking of the polymer side chains (6, 35). We show that blending P3HT with another thermally stable HTL material, copper phthalocyanine (CuPc), followed by a postdeposition solvent-annealing

step produced highly crystalline films with excellent hole transport characteristics.

Details of the HTL optimization process and film characterization are provided in the supplementary materials (see figs. S1 to S6). To summarize the key results, x-ray diffraction (XRD) analysis revealed that applying a solvent-annealing treatment with chlorobenzene to pure P3HT films improved crystallinity and conductivity compared with untreated films, and both properties were further improved by blending P3HT with CuPc (fig. S1). When incorporated into a baseline meso- TiO_2 PSC process as a substitute for Spiro-OMeTAD (fig. S4 shows the device structure), the best results were obtained for a 10:1 (v/v) ratio blend of P3HT (12 mg/ml):CuPc (5 mg/ml) (fig. S5). The average FF for cells with the optimized P3HT:CuPc blend was 0.790 ± 0.016 , compared with 0.728 ± 0.016 for as-deposited P3HT films, and the average PCE for the optimized cells was $20.83 \pm 0.55\%$ (fig. S6). This performance compared favorably to conventional meso- TiO_2 -based cells using Spiro-OMeTAD or PTAA as the HTL, as reported previously (10, 12, 24, 25).

For electron extraction, the most widely used ETL configuration for n-i-p PSCs consists of a thin ($\sim 50 \text{ nm}$), compact TiO_2 layer (c- TiO_2) covered by a meso- TiO_2 layer of typical thickness $>100 \text{ nm}$. Dense random arrays of TiO_2 nanowires grown by solution methods have also been explored as an alternative to meso- TiO_2 but with negligible performance benefit (36–38). The main role of the meso- TiO_2 (or

random nanowire array) layer is to provide a scaffold for the perovskite film to form a dense, pinhole-free film. These layers may also contribute to charge carrier collection, but the large contact area between the meso- TiO_2 (or random nanowire array) and the perovskite can also result in substantial interface recombination. Therefore, some form of passivation is required to achieve high voltages. A thin passivating interlayer of PMMA:PCBM can effectively increase the V_{oc} of meso- TiO_2 -based cells (10, 12, 39, 40), but this layer must be ultrathin to limit resistive losses.

The average performance of meso- TiO_2 -based cells with the structure glass/ITO/c- TiO_2 /meso- TiO_2 /PMMA:PCBM/ $\text{Cs}_{0.05}\text{FA}_{0.88}\text{MA}_{0.07}\text{PbI}_{2.56}\text{Br}_{0.44}$ /PMMA/P3HT:CuPc/Gold, where the ratio of PMMA:PCBM mixed precursor solution is 1:3 (w/w), is shown in Fig. 2 and replotted in fig. S6 for the optimized P3HT:CuPc blend discussed above (referred to as meso- TiO_2 in the remainder of this work). Here, ITO refers to indium-doped tin oxide, and MA and FA are methylammonium and formamidinium, respectively. The band gap of the perovskite we used throughout was $\sim 1.6 \text{ eV}$ (fig. S7). We also fabricated planar n-i-p cells with just the c- TiO_2 ETL layer, omitting the meso- TiO_2 layer altogether. Cell data are shown in Fig. 2 for planar cells fabricated with a solution-processed c- TiO_2 layer (“S-Planar”) and an atomic-layer deposition (ALD) c- TiO_2 layer (“A-Planar”), with all other layers identical to the meso- TiO_2 cell. Note that the average V_{oc} of the planar cells is slightly higher than that of the meso- TiO_2 cells (Fig. 2C) and is likely the result of the smaller interface area over which recombination can occur. The reduced FF in the planar c- TiO_2 case (Fig. 2E), however, is likely the result of a more uniform passivation layer compared with the meso- TiO_2 ETL. The higher FF of the meso- TiO_2 may result from partial or nonuniform coverage of the passivating layer on the textured ETL surface that has thinner regions with more efficient charge conduction through an otherwise poorly conducting film.

Comparison between the planar c- TiO_2 and the meso- TiO_2 ETL interfaces suggested that there exists a tradeoff between V_{oc} and FF that is mediated by the continuity of coverage of the passivation layer. On the basis of this finding, we developed a nanopatterned ETL consisting of an array of TiO_2 nanorods on a planar c- TiO_2 layer. This optimized texture enables the high V_{oc} of the planar architecture while providing efficient charge extraction and thus high FF. The ETL fabrication process is illustrated in fig. S8. Starting with a glass/ITO/c- TiO_2 substrate, we first deposited a PMMA resist layer by spin coating, followed by a 15-min annealing step. The nanorod array was defined in the resist using electron-beam lithography (EBL), and the pattern was developed in a solution of methyl isobutyl ketone

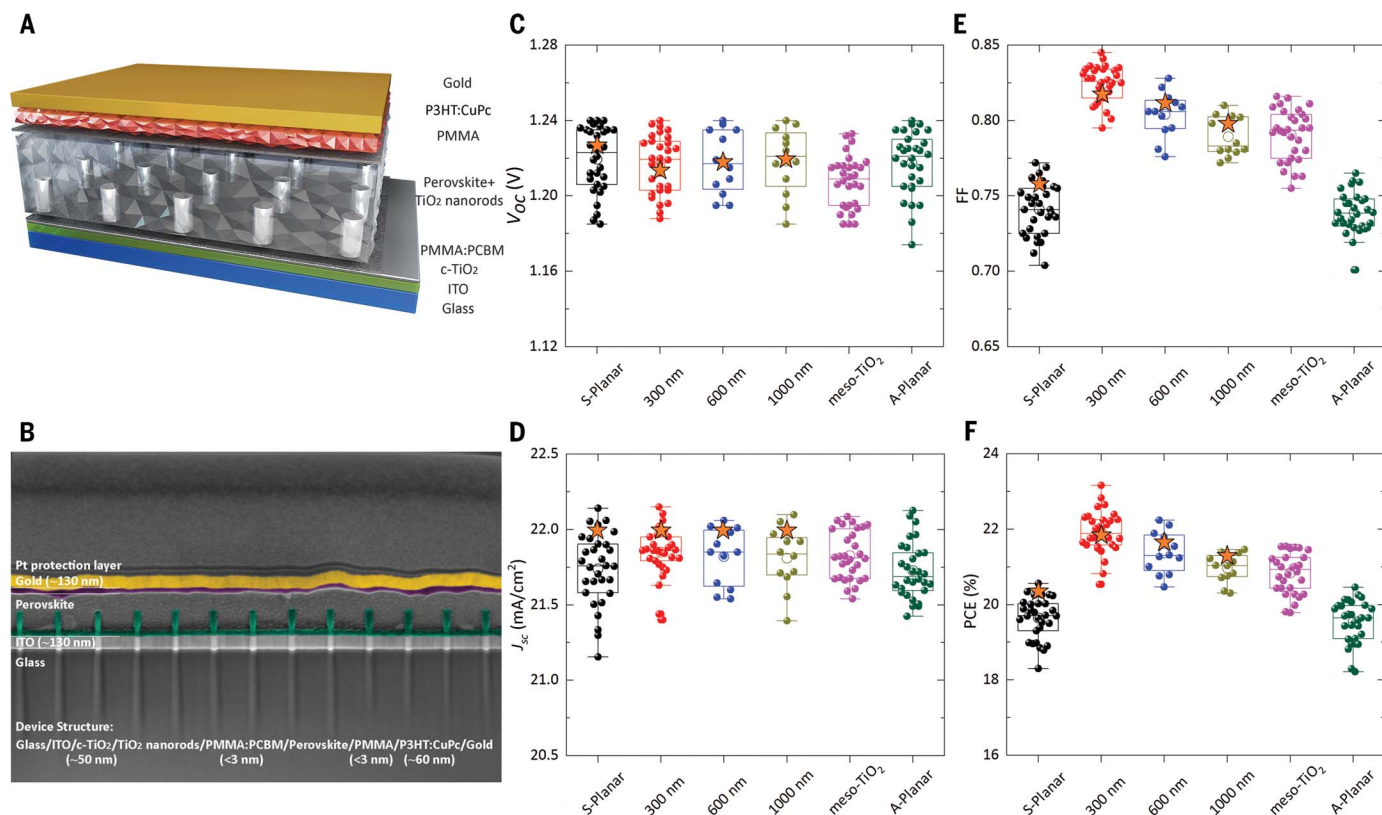


Fig. 2. Nanostructured TiO₂ ETL and statistical distribution of the photovoltaic parameters for nanopattern and control perovskite cells. (A) Schematic of nanopattern perovskite cell studied in this work. (B) Cross-sectional SEM image of the nanopattern cell structure [note that the perovskite layer was fabricated using ~1 mol/ml diluted precursor solution instead of the standard ~1.3 mol/ml (for cells); the Pt protection layer was only used to prepare the focused ion beam SEM cross-sectional image]. (C) Distribution of V_{oc} . (D) Distribution of J_{sc} . (E) Distribution of FF. (F) Distribution of PCE. Note that the control cells are

S-Planar, meso-TiO₂, and A-Planar; the nanopattern cells are 300, 600, and 1000 nm. S-Planar represents planar cells based on solution-processed compact TiO₂ ETLs. meso-TiO₂ represents mesoporous cells based on solution-processed compact TiO₂/mesoporous TiO₂ ETLs. A-Planar represents planar cells based on ALD-deposited compact TiO₂ ETLs. “300 nm,” “600 nm,” and “1000 nm” represent the nanopattern cells based on nanostructured TiO₂ nanorods with a spacing of 300, 600, and 1000 nm, respectively. The orange star icons indicate the values calculated from the 3D numerical simulations.

(MIBK) and isopropyl alcohol (IPA). The entire sample was then coated with an ALD-deposited conformal TiO₂ layer that filled the holes in the PMMA resist and covered the resist between the holes. Finally, the TiO₂-capping layer was etched with inductively coupled plasma-reactive ion etching (ICP-RIE) until the resist surface was exposed, and the remaining resist was removed by oxygen plasma. After etching, the TiO₂ nanorod substrates were annealed at 500°C for 30 min under dry air before further processing, converting the as-deposited amorphous TiO₂ into a nanocrystalline anatase material.

Although the diameter, pitch (spacing), and height of the nanorods could all influence the cell performance, we set the diameter to 50 nm and the height to 200 nm and focused on investigating the impact of pitch. This approach was motivated by device simulations (described below) that predicted the largest changes in device performance through modification of local contact spacing. Figures S9 and S10 show the nanopatterned TiO₂ ETL with

itches of 300, 600, and 1000 nm. The nanopatterned perovskite cell structure was ITO/c-TiO₂/TiO₂ nanorods/PMMA:PCBM/Cs_{0.05}FA_{0.88}MA_{0.07}PbI_{2.56}Br_{0.44}/PMMA/P3HT:CuPc/Gold (Fig. 2, A and B).

To evaluate the performance enhancement provided by the nanopatterned ETL, in Fig. 2, we compare the nanopatterned cells with different pitches with three control cell architectures, meso-TiO₂, A-Planar, and S-Planar. The two different planar cell types were included to compare the solution and ALD-deposited materials because the nanorods were ALD deposited and both compact layers for the meso-TiO₂ and nanopatterned cells were solution deposited; the deposition method had a negligible impact on the cell performance. All of the cells include double-side passivation with ultrathin films of PMMA and PMMA:PCBM blends at the perovskite-HTL and perovskite-ETL interfaces, respectively (10, 11).

All six cell architectures demonstrated excellent surface passivation quality (Fig. 2C), with an average V_{oc} > 1.2 V and maximum

V_{oc} ~1.24 V. The nanopatterned cells achieved V_{oc} values equivalent to those of the planar cells for 300-, 600-, and 1000-nm nanorod pitches, with average V_{oc} values of 1.217 ± 0.015 , 1.218 ± 0.017 , and 1.218 ± 0.018 V, respectively, showing that the nanorods did not affect the passivation quality compared with planar cells. Also, J_{sc} was similar for all six cell architectures (Fig. 2D), with average values ranging from 21.73 ± 0.19 mA/cm² (A-Planar) to 21.85 ± 0.17 mA/cm² (300 nm).

A comparison of representative current-voltage (J - V) curves for planar and nanopatterned cells shows that the FF increase with nanorods was dominated by reduced series resistance (Fig. 3A). The planar cells had the lowest average FFs of 0.741 ± 0.017 (S-Planar) and 0.739 ± 0.013 (A-Planar), whereas the meso-TiO₂ cells had FF = 0.790 ± 0.017 (Fig. 2E). By contrast, the optimum nanopatterned cells with 300-nm pitch had an average FF = 0.824 ± 0.012 , which decreased to 0.803 ± 0.015 for 600-nm pitch and 0.789 ± 0.013 for 1000-nm pitch. The 300-nm pitch nanopatterned cells

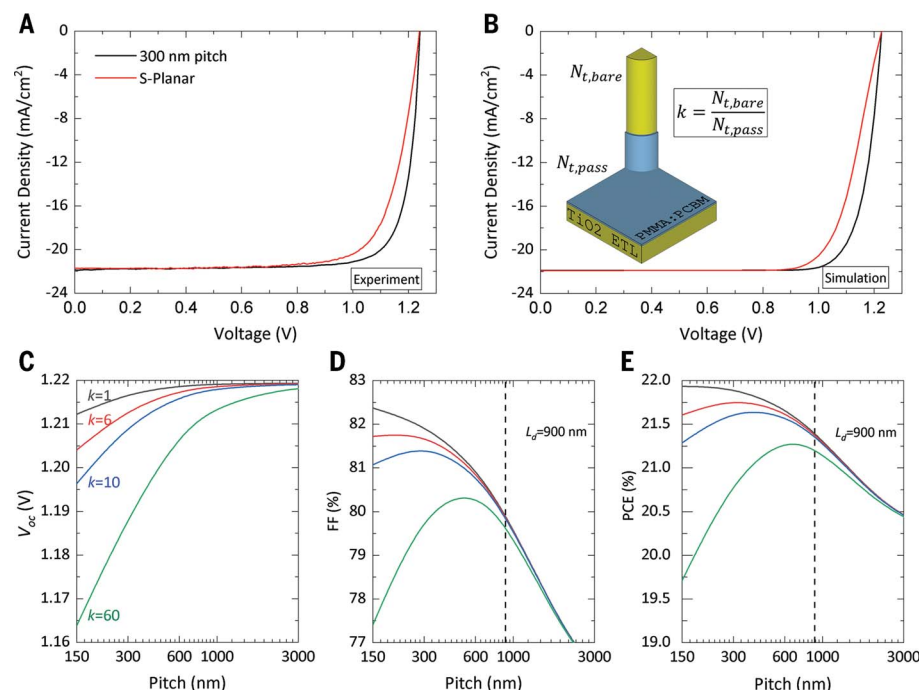


Fig. 3. Simulation results. (A) Experimental *J-V* curves of the S-Planar (reference cell) and the 300-nm pitch, representing midperformance cells from each batch. (B) Simulated *J-V* curves for the planar and nanostructured cell in which we presume that only 30% of the nanorod is coated with the insulating passivation layer (inset). The periodic separation of the nanorods, or pitch, governs V_{oc} (C), FF (D), and thus overall efficiency (E). The unpassivated and passivated ETL surfaces are characterized by defect concentrations, $N_{t,bare}$ and $N_{t,pass}$, respectively. (C) to (E) plot the dependence of cell performance on the ratio of unpassivated to passivated defect density, k , for CF = 30%, illustrating that the optimum pitch depends on the strength of unpassivated interface recombination. The electron diffusion length, L_d , is marked by vertical dashed lines.

had an average PCE of $21.91 \pm 0.57\%$, compared with $19.64 \pm 0.55\%$ ($19.54 \pm 0.56\%$) for the S-Planar (A-Planar) cells and $20.83 \pm 0.55\%$ for the meso-TiO₂ cells (Fig. 2F). The best-performing nanopatterned cell had a PCE of 23.17% with $V_{oc} = 1.240$ V and FF = 0.845 (fig. S11).

There are several possible explanations for the combination of outstanding passivation (V_{oc}) and charge extraction/transport (FF) provided by the nanopatterned ETL, including: (i) improvements in the optoelectronic quality of the perovskite film when it is deposited on the nanopatterned substrate; (ii) modification of the passivation layer coverage and/or thickness at the ETL-perovskite interface resulting in an improved balance of passivation and charge transport across the interface; and (iii) improved charge collection and interface transport caused by the geometry of the nanorods. For possibility (i), the nanorods could scaffold the growth of the perovskite film, but we found no evidence of morphology changes from scanning electron microscope (SEM) images of perovskite films deposited on planar, nanopatterned and meso-TiO₂ ETLs (fig. S12), nor did we find appreciable differences in crystal structure, orientation, or crystallinity

from XRD measurements of films on the different substrates (fig. S13). Photoluminescence (PL; steady-state and time-resolved) measurements of films deposited on the different ETL structures were consistent with the experimental cell V_{oc} values: The planar and nanopatterned cells showed almost identical steady-state intensity and PL decay curves, whereas the meso-TiO₂ sample had a slightly lower PL intensity and faster decay, indicating increased recombination losses (fig. S14). Thus, the nanopatterned ETL had a minimal impact on the physical and optoelectronic properties of the perovskite film.

To test explanations (ii) and (iii) above, we developed a full 3D numerical drift-diffusion model of the n-i-p PSC including the periodic nanostructured TiO₂ nanorods (fig. S15). The resistive PMMA:PCBM layer at the perovskite-TiO₂ interface was introduced in the model as a 3-nm-thick insulating interlayer. The valence and conduction band energy levels of this interlayer are aligned to those of the perovskite and ETL, respectively, to avoid introducing energy barriers to charge transport. Bulk conductivity of the layer was reduced to match the FF of the S-Planar control samples. Nonradiative recombination at this interface and in the

perovskite bulk was modeled with generalized Shockley-Read Hall statistics (41), parameterized by self-consistent time-resolved (TR) fitting to TRPL data measured for a bare perovskite film on glass, and a perovskite film deposited on a planar glass/ITO/TiO₂/PMMA:PCBM substrate (fig. S16).

From these fits, we extracted a bulk perovskite defect density of $2 \times 10^{14} \text{ cm}^{-3}$ for an effective electron lifetime of ~ 600 ns. This value corresponds well with recent results from Ni *et al.* (42), who extracted bulk defect concentrations of $\sim 10^{14}$ to 10^{15} cm^{-3} in a range of multicrystalline perovskite films from independent capacitance-based techniques. We fit a charge-carrier mobility of $0.5 \text{ cm}^2/\text{V}\cdot\text{s}$ for a corresponding diffusion length of ~ 900 nm at 1 sun-equivalent injection levels (fig. S17). The fitted surface areal defect density at the PMMA:PCBM-passivated interface was $5 \times 10^8 \text{ cm}^{-2}$, for an equivalent surface-recombination velocity of only 3 cm/s, indicative of the high-quality passivation achieved with this method. These parameters were integrated into the full 3D cell simulations, predicting V_{oc} and FF consistent with the experimental results (fig. S18). Details of the TRPL and cell models and associated simulation parameters are provided in the supplementary materials.

With this model, we initially tested possibility (iii), which presumed that the TiO₂ nanorods increased the effective surface area of the ETL and reduced resistance. Our simulations showed that if the TiO₂ nanorod was conformally coated by the passivation interlayer, then the increased surface area could not account for the enhancement in FF (fig. S19) and actually led to a marginal decrease in V_{oc} (~ 8 mV) and FF ($\sim 0.08\%$) for the 300 nm compared with the S-Planar cell because of the increase in surface area at which nonradiative recombination can occur. FF did not increase because collection efficiency in the perovskite bulk was near unity as the predicted charge carrier diffusion lengths (900 nm) are more than double the absorber thickness of 400 nm.

For possibility (ii), we presumed that the nanostructure influenced conformity of the PMMA:PCBM layer across the TiO₂-perovskite interface, which was deposited from solution by spin-coating. Some faces of the nanostructured rods likely had thinner or noncontinuous layers of PMMA:PCBM or both, for example, at the radially outward or top faces of the rod. We show this schematically in the inset of Fig. 3B. The uniformity of PMMA:PCBM at the TiO₂ nanorods could not be observed given that the PMMA:PCBM film was <3 -nm thick and offered insufficient contrast to observe with electron microscopy. Instead, we simulated imperfect PMMA:PCBM coverage by assuming a coverage fraction (CF) of 30% of the TiO₂ nanorod sidewalls and presumed that the bare TiO₂-perovskite interface had a defect density

one order of magnitude higher than the passivated surface at $5 \times 10^9 \text{ cm}^{-2}$. A discussion of these assumptions is provided in the supplementary materials. Under these conditions, we found close agreement between simulation and experimental results for both the magnitude of the FF change between the S-Planar and 300-nm cases (Fig. 3B) and the change in FF with the nanorod pitch, as indicated by the star markers in Fig. 2E. The corresponding V_{oc} is only marginally affected, and overall device efficiency was consistent with experimental results (Fig. 2, C and F).

Our device simulations suggest that the formation of repeatable nanoscale regions of an unpassivated nanorod TiO_2 -perovskite interface facilitate localized low-resistance charge transport with limited impact on effective interface recombination and V_{oc} . This localized contact structure approach is analogous to local contact structures used in high-efficiency laboratory and industrial silicon solar cells, in which local openings in electrically passivating and insulating dielectric layers are laser micro-machined or chemically etched (30, 31, 43). In both cases, a global optimum trades off interface recombination (V_{oc}) and charge extraction (FF) (Fig. 3, C and D). When nonradiative recombination was increased at the unpassivated nanorod surfaces, expanding pitch reduced the effective interface recombination and increased V_{oc} . However, FF was maximized at an intermediate pitch. For small pitches, the increased recombination that reduced V_{oc} also reduced FF, whereas larger pitches reduced FF through increased transport resistance in the perovskite bulk. The convolution of FF and V_{oc} across pitches showed that a narrow pitch range optimized performance, which in our parameterization fell near the 300-nm pitch we used (Fig. 3E). Our experimental exploration of the cell structure focused on rod separation because in our device simulations (fig. S20) modification of rod height and diameter led to much smaller increases or, in some cases, decreases of V_{oc} and FF.

The results presented above were all obtained on cells of area 0.165 cm^2 , but we also fabricated optimized 300-nm-pitch nanopatterned cells with an effective area of 1.2 cm^2 and $J-V$ data measured with an $\sim 1.02\text{-cm}^2$ aperture mask. Our champion perovskite cell exhibited a PCE of 21.96% (21.86%) with $V_{oc} \sim 1.205 \text{ V}$ (1.204 V), $J_{sc} \sim 21.80 \text{ mA/cm}^2$ (21.86 mA/cm^2), and FF ~ 0.836 (0.836) from reverse (forward) scans measured in-house (Fig. 4A). External quantum efficiency (EQE) spectra confirmed the measured photocurrent with a relative discrepancy of $\sim 3\%$ between the integrated J_{sc} from the EQE and the J_{sc} measured from the $J-V$ curve (Fig. 4B). Another cell submitted to an independent testing center achieved a certified efficiency of $21.698 \pm 0.555\%$ with FF of $83.87 \pm 1.16\%$ (fig. S21).

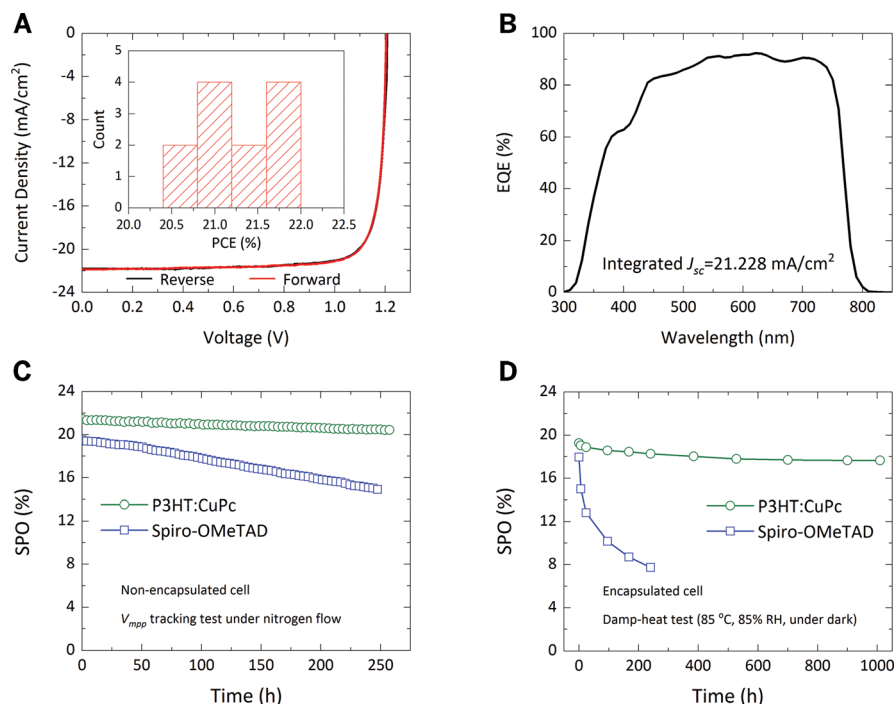


Fig. 4. Device performance and long-term stability tests for 1-cm² perovskite cells. (A) $J-V$ performance. (B) EQE measurement. (C) SPO of nonencapsulated cells based on P3HT:CuPc and Spiro-OMeTAD HTL measured by V_{mpp} tracking under continuous 1 sun illumination intensity. (D) SPO of encapsulated cells based on P3HT:CuPc and Spiro-OMeTAD HTL. Note that the cell structure for the damp heat tests included a MoO_x -ITO barrier between the HTL and the gold electrode: ITO/c- TiO_2 /TiO₂ nanorods/PMMA:PCBM/ $\text{Cs}_{0.05}\text{FA}_{0.88}\text{MA}_{0.07}\text{PbI}_{2.56}\text{Br}_{0.44}$ /PMMA/P3HT:CuPc (or Spiro-OMeTAD)/ MoO_x ($\sim 10 \text{ nm}$)/IZO ($\sim 40 \text{ nm}$)/gold.

The histogram distribution figure (inset, Fig. 4A) presents the reproducibility of the large-area perovskite cells (details of the $J-V$ parameters are provided in table S1). The $\sim 30\text{-mV}$ decrease in V_{oc} when we used the aperture to measure the cell compared with the $J-V$ performance measured without an aperture (fig. S22) was ascribed to carrier recombination within the cell's dark region shaded by the mask (44). Taking this deficit into account, we conclude that there was negligible loss in V_{oc} or FF between cells of area 0.165 and 1 cm^2 despite a $>6\times$ increase in photocurrent.

To test the light and thermal stability of the cells, we conducted two extended degradation tests: a steady-state power output (SPO) measurement [unencapsulated cells held at maximum power point voltage (V_{mpp}) under continuous illumination in a N_2 atmosphere] and a damp heat test (encapsulated cells exposed to 85°C and 85% relative humidity in the dark). For the SPO test, Fig. 4C shows that the cell with the P3HT:CuPc HTL retained $\sim 95.3\%$ of its initial efficiency (PCE_{initial} $\sim 21.45\%$) after 260 hours, whereas the control cell with a Spiro-OMeTAD HTL dropped to $\sim 76.1\%$ of its initial efficiency (PCE_{initial} $\sim 19.50\%$) after 250 hours. In the damp heat test results (Fig. 4D), the P3HT:CuPc-based cell

retained $\sim 91.7\%$ of its initial efficiency after 1009 hours of damp heat exposure, whereas the cell with the Spiro-OMeTAD HTL exhibited substantial degradation after only 240 hours, which we attributed to the severe deterioration at the interface between perovskite and Spiro-OMeTAD caused by lithium ion diffusion (6, 32, 33). The cells used for the damp heat tests included an additional barrier layer consisting of MoO_x ($\sim 10 \text{ nm}$) and IZO ($\sim 40 \text{ nm}$) placed between the HTL and the gold electrode to prevent gold diffusion into the cell at elevated temperatures (45).

Although we only present here stability data for one control and one nanopatterned cell, the same tests were repeated on multiple cell types incorporating the P3HT:CuPc HTL, all of which exhibited a similar improvement in stability relative to Spiro-OMeTAD-based cells. The hydrophobic and thermally stable nature of the ionic dopant-free P3HT:CuPc HTLs could increase the stability of perovskite cells compared with ionic-doped organic HTL materials without any penalty in performance. Time-dependent power output and $J-V$ curves showing the cell performance evolution during the two degradation tests are provided in figs. S23 to S26.

Although the nanopatterned ETL reported here was fabricated with EBL, the structure is

compatible with commercial scale fabrication using nanoimprint techniques (46). Some form of self-assembled ETL nanostructure might also provide a sufficiently irregular surface to form local contacts through a passivation layer. More generally, our work demonstrates the important interaction among ETL morphology, interface passivation, and charge transport at the ETL-perovskite interface.

REFERENCES AND NOTES

- National Renewable Energy Laboratory, U.S. Department of Energy, "NREL efficiency chart" (2020); www.nrel.gov/pv/assets/pdfs/best-research-cell-efficiencies.20200311.pdf.
- J. Burschka et al., *Nature* **499**, 316–319 (2013).
- N. J. Jeon et al., *Nature* **517**, 476–480 (2015).
- W. S. Yang et al., *Science* **348**, 1234–1237 (2015).
- W. S. Yang et al., *Science* **356**, 1376–1379 (2017).
- E. H. Jung et al., *Nature* **567**, 511–515 (2019).
- M. A. Green et al., *Prog. Photovolt. Res. Appl.* **27**, 3–12 (2019).
- M. A. Green et al., *Prog. Photovolt. Res. Appl.* **27**, 565–575 (2019).
- M. A. Green et al., *Prog. Photovolt. Res. Appl.* **28**, 3–15 (2019).
- J. Peng et al., *Energy Environ. Sci.* **10**, 1792–1800 (2017).
- J. Peng et al., *Adv. Energy Mater.* **8**, 1801208 (2018).
- S.-H. Turren-Cruz, A. Hagfeldt, M. Saliba, *Science* **362**, 449–453 (2018).
- Q. Wang, Q. Dong, T. Li, A. Gruverman, J. Huang, *Adv. Mater.* **28**, 6734–6739 (2016).
- L. Zuo et al., *Sci. Adv.* **3**, e1700106 (2017).
- C. Tao et al., *Energy Environ. Sci.* **8**, 2365–2370 (2015).
- F. Zhang et al., *Adv. Mater.* **29**, 1606806 (2017).
- J. Xu et al., *Nat. Commun.* **6**, 7081 (2015).
- D. Koushik et al., *Energy Environ. Sci.* **10**, 91–100 (2017).
- J.-P. Correa-Baena et al., *Energy Environ. Sci.* **10**, 1207–1212 (2017).
- S. Gharibzadeh et al., *Adv. Energy Mater.* **9**, 1803699 (2019).
- M. A. Mahmud et al., *Adv. Funct. Mater.* **30**, 1907962 (2020).
- D. Luo et al., *Science* **360**, 1442–1446 (2018).
- X. Zheng et al., *Nat. Energy* **5**, 131–140 (2020).
- Q. Jiang et al., *Nat. Photonics* **13**, 460–466 (2019).
- J. J. Yoo et al., *Energy Environ. Sci.* **12**, 2192–2199 (2019).
- M. J. Kerr, A. Cuevas, *Semicond. Sci. Technol.* **17**, 35–38 (2001).
- J. Shewchun, R. Singh, M. Green, *J. Appl. Phys.* **48**, 765–770 (1977).
- Y. Wu et al., *Adv. Mater.* **29**, 1701073 (2017).
- T. Matsui et al., *Adv. Mater.* **31**, e1806823 (2019).
- E. Franklin et al., *Prog. Photovolt. Res. Appl.* **24**, 411–427 (2014).
- M. A. Green, *Prog. Photovolt. Res. Appl.* **17**, 183–189 (2009).
- H. Min et al., *Science* **366**, 749–753 (2019).
- Y. Hou et al., *Science* **358**, 1192–1197 (2017).
- Q.-Q. Chu et al., *J. Mater. Sci. Technol.* **35**, 987–993 (2019).
- Q. Hu et al., *Solar RRL* **3**, 1800264 (2019).
- L. Yang et al., *J. Colloid Interface Sci.* **534**, 459–468 (2019).
- A. Fakhruddin et al., *ACS Nano* **9**, 8420–8429 (2015).
- X. Li et al., *ACS Appl. Mater. Interfaces* **8**, 21358–21365 (2016).
- A. J. Bett et al., *Prog. Photovolt. Res. Appl.* **28**, 99–110 (2020).
- C. Wu et al., *Solar RRL* **2**, 1800052 (2018).
- W. Shockley, W. T. Read Jr., *Phys. Rev.* **87**, 835–842 (1952).
- Z. Ni et al., *Science* **367**, 1352–1358 (2020).
- S. Zhang et al., *IEEE J. Photovolt.* **6**, 145–152 (2016).
- D. Kiermasch, L. Gil-Escrig, H. J. Bolink, K. Tvingstedt, *Joule* **3**, 16–26 (2019).
- T. Duong et al., *Sol. Energy Mater. Sol. Cells* **188**, 27–36 (2018).
- L. J. Guo, *Adv. Mater.* **19**, 495–513 (2007).

ACKNOWLEDGMENTS: Funding: This work was supported by the Australian Government through the Australian Renewable Energy Agency (ARENA) and the Australian Research Council. Responsibility for the views, information, or advice expressed herein is not accepted by the Australian Government. J.P. acknowledges the financial support of a postdoctoral fellowship from the Australian

Centre for Advanced Photovoltaics (ACAP). T.P.W. is the recipient of an Australian Research Council Future Fellowship (project no. FT180100302) funded by the Australian Government. T.P.W. also acknowledges the support of the Open Fund of the State Key Laboratory of Optoelectronic Materials and Technologies (Sun Yat-sen University). Y.R., Q.L., and J.L. acknowledge funding from the National Natural Science Foundation of China (grant nos. 11974436 and 11674402) and the Guangdong Basic and Applied Basic Research Foundation (grant no. 2020B1515020019). **Author contributions:** J.P. conceived the idea, designed the overall experiments, and led the project. J.P., Y.W., T.D., M.A.M., and H.S. prepared and characterized the perovskite cell devices. D.W., T.P.W., and K.J.W. conducted the 3D numerical simulation. Y.R. and Q.L. performed the PMMA hole pattern fabrication. J.L. supervised the PMMA hole pattern fabrication and optimization. J.P. and D.-Y.C. performed ALD TiO₂ deposition and ICP-RIE etching. Y.W. and M.A.M. performed the GIXRD and XRD measurements and analysis. M.T. and H.T.N. performed the PL and TRPL measurements and analysis. T.D., O.L.C.L., and S.Z. conducted the SEM measurements and analysis. T.L. and Y.L. performed the AFM measurements and analysis. W.L. performed the EQE measurements. L.L. and F.K. performed the FIB-SEM measurements and analysis. J.P., D.W., and T.P.W. wrote and revised the manuscript. T.P.W. and K.R.C. supervised the project. All authors contributed to the discussion of the results and revision of the manuscript. **Competing interests:** The authors declare no competing interests. **Data and materials availability:** All data needed to evaluate the conclusions in the paper are available in the main text or the supplementary materials.

SUPPLEMENTARY MATERIALS

science.sciencemag.org/content/371/6527/390/suppl/DC1
Materials and Methods
Supplementary Text
Figs. S1 to S27
Table S1
References (47–60)
3D Simulation Model File

24 March 2020; resubmitted 18 October 2020
Accepted 10 December 2020
10.1126/science.abb8687

Nanoscale localized contacts for high fill factors in polymer-passivated perovskite solar cells

Jun PengDaniel WalterYuhao RenMike TebyetekerwaYiliang WuThe DuongQiaoling LinJuntao LiTeng LuMd Arafat MahmudOlivier Lee Cheong LemShenyou ZhaoWenzhu LiuYun LiuHeping ShenLi LiFelipe KremerHieu T. NguyenDuk-Yong ChoiKlaus J. WeberKylie R. CatchpoleThomas P. White

Science, 371 (6527), • DOI: 10.1126/science.abb8687

Opening charge transport pathways

In perovskite solar cells, the insulating nature of passivation layers needed to boost open-circuit voltage also increases the series resistance of the cell and limits the fill factor. Most improvements in power conversion efficiency have come from higher open-circuit voltage, with most fill factor improvements reported for very small-area cells. Peng *et al.* used a nanostructured titanium oxide electron transport layer to boost the fill factor of larger-area cells (1 square centimeter) to 0.84 by creating local regions with high conductivity.

Science, this issue p. 390

View the article online

<https://www.science.org/doi/10.1126/science.abb8687>

Permissions

<https://www.science.org/help/reprints-and-permissions>

Use of this article is subject to the [Terms of service](#)